Global Distribution of Asian, Middle Eastern, and Saharan Dust Simulated by CESM1/CARMA

Siying Lian[1], Luxi Zhou[2], Daniel M. Murphy[3], Karl D. Froyd[3], Owen B. Toon[4], and Pengfei Yu[1*]

[1]Institute for Environmental and Climate Research, Jinan University, Guangzhou, China

[2]Guangzhou Institute of Tropical and Marine Meteorology, CMA, Guangzhou, China

[3]Chemical Science Laboratory, National Oceanic and Atmospheric Administration, Boulder, Colorado

[4]Department of Atmospheric and Oceanic Sciences and Laboratory for Atmospheric and Space Physics, University of Colorado, Boulder, Colorado

Corresponding author: Pengfei Yu (pengfei.yu@colorado.edu)

11   **Abstract.** Dust aerosols affect the radiative and energy balance at local and global scales by scattering

12   and absorbing sunlight and infrared light. Parameterizations of dust lifting, microphysics, as well as

13   physical and radiative properties of dust in climate models are still subject to large uncertainty. Here

14   we use a sectional aerosol model (CARMA) coupled with a climate model (CESM1) to investigate the

15   global distribution of dust aerosols, with an emphasis on the vertical distribution of dust. Consistent

16   with observations at locations remote from source regions, simulated dust mass size distributions peak

17   at around 2-3 micrometres in diameter and increase by 4 orders of magnitude from 0.1 µm to 2 µm.

18   The size distribution above 2 µm is highly variable depending on distance from the source, and subject

19   to uncertainty due to possible size dependent changes in physical properties such as shape and density.

20   Simulated annual mean dust mass concentrations are within one order of magnitude of those found by

21   the surface measurement network around the globe. Simulated annual mean aerosol optical depths are

22   ~10% lower than AERONET observations near the dust source regions. Both simulations and in-situ

23   measurements during the NASA ATom field campaign suggest that dust mass concentrations over the

24   remote ocean drop by two to three orders of magnitude from the surface to the upper troposphere (200

25   hPa). The model suggests that Saharan, Middle Eastern, and Asian dust accounts for ~59.7%, 12.5%,

26   and 13.3% of the global annual mean dust emissions, with the remaining 14.5% originating from

27   scattered smaller dust sources. Although Saharan dust dominates global dust mass loading at the

28   surface, the relative contribution of Asian dust increases with altitude and becomes dominant in the

29   upper troposphere. The simulations show that Asian dust contributes ~60.9% to the global and annual

30   mean dust concentration between 266 hPa and 160 hPa. Asian dust is mostly lifted in the spring by

31   mid-latitude frontal systems. However, deep convection during the Asian summer monsoon (ASM)

32   favours the vertical transport of local dust to the upper atmosphere. Simulated dust accumulates in the

33   ASM anticyclone and forms a local maximum; however, the simulated dust mass concentration is only

34   ~0.04% of the total aerosols in the Asian Tropopause Aerosol Layer (ATAL), which are dominated by

35   organics, sulfates and nitrates.

1 Introduction

Mineral dust, from both natural and anthropogenic sources, accounting for more than 50% of the total global aerosol mass burden (Textor et al., 2006; Andreae, 1995; Andreae et al., 1986; Zender et al., 2004). Mineral dust impacts the radiation balance of the planet by scattering and absorbing sunlight, and unlike most other types of aerosols, dust has significant effects on thermal radiation due to its relatively large particle sizes (i.e., Satheesh and Moorthy, 2005; Sokolik and Toon, 1996; Balkanski et al., 2007; Tegen and Lacis, 1996). Dust optical properties vary between different sources (Sokolik and Toon, 1999), making it complex to construct global models of dust radiative effects. Dust also indirectly impacts climate by serving as a prominent nuclei for heterogenous ice formation (e.g., Maloney et al., 2022; Cziczo et al., 2013). Despite being insoluble, dust can also serve as cloud condensation nuclei due to the large particle sizes of dust, influencing cloud microphysical and rainfall processes (Rosenfeld et al., 2001; Levin et al., 1996). The climate effects of mineral dust are profound because it can be entrained into the boundary layer and transported long distances (Grousset et al., 2003; Prospero, 1996). Tegen and Schepanski (2009) suggest that the Sahara and Asia are the largest source regions of mineral dust on Earth, accounting for more than 60-95% of the global dust load. Saharan dust is lifted all year, primarily due to subtropical weather systems. Saharan dust can travel across the Atlantic Ocean, driven by the trade wind circulation (Karyampudi, 1979; Karyampudi et al., 1999). Asian dust is mostly lifted in the spring by mid-latitude frontal systems, and is likely to be removed near its source due to rainfall though it can be carried at upper levels across the Pacific (Su and Toon, 2011). The North African and Asian dust can be transported to the upper troposphere (UT) and even farther around the Earth by subtropical westerly jets (Yang et al., 2022). The contributions of dust from the different source regions to the global dust load are still uncertain. Global model simulations show that the dust emission from different sources regions differ by an order of magnitude among different models (Huneeus et al., 2011). Kok et al. (2021) suggests that current models on average overestimate the contribution of North African dust to the global burden by ~65%, while underestimating the contribution of Asian dust by ~30%.

Long-term in situ measurement of dust aerosols over source regions and oceanic regions affected by transport has been conducted at only a few sites in the last several decades (Schulz et al., 2012; Rodriguez et al., 2012). For example, the emission and surface concentration of dust have been

65 measured in Barbados from 1965 to the present (Prospero and Lamb, 2003; Prospero and Nees, 1986).

66 These measurements suggest that dust mass concentration increased by a factor of four from the 1960s

67 to 1980s. The measurements include data obtained from cruises and monitoring sites. Monthly mineral

68 dust concentration measurements are available at numerous marine sites around the globe from 1972 to

69 1998, taken by the Rosenstiel School of Marine and Atmospheric Science at the University of Miami

70 (Prospero, 1989; Arimoto et al., 1996). In addition to surface measurements, a number of studies

71 characterize dust concentration using visibility from ground-level meteorological observation systems

72 (Wang et al., 2008; Chepil and Woodruff, 1957; Mohamed and Frangi, 1986; d'Almeida, 1986). But

73 these long-term monitoring stations alone do not provide enough observational constraints for a

74 comprehensive quantification of dust loads in the full atmosphere (lower, middle and upper

75 troposphere) and an understanding of their associated impacts and processes (Knippertz and Todd,

76 2012).

77   Measurements of the vertical distribution of dust are crucial for understanding the vertical and

78 long-distance transport of dust aerosols. Bourgeois et al. (2015) showed that the residence time of dust

79 is significantly affected by its vertical location during long-range transport. Colarco et al. (2003)

80 showed that the sedimentation and downward vertical winds significantly affect Saharan dust's vertical

81 profile across the North Atlantic Ocean. However, in-situ measurements of dust's vertical distribution

82 from the surface to the upper troposphere are extremely limited compared with surface measurements.

83 Remote sensing techniques including lidars and satellites are used to explore the vertical distribution of

84 dust aerosols in the atmosphere (Murayama et al., 2001;Di Sarra et al., 2001). Yu et al. (2015a)

85 calculated the vertical mass flux of dust by converting the dust extinction coefficient of CALIOP to

86 dust mass concentration, yielding estimated dust mass fluxes with an uncertainty of ± (45-70%). Kim et

87 al. (2019) deduced the vertical profiles of dust aerosols over Asia and the North Pacific using five

88 global models that participated in the AeroCom phase II, the dust optical depth (DOD) provided by

89 multiple satellite and ground-based measurements, which revealed a longitudinal gradient during trans-

90 Pacific transport. Based on CloudSat satellite data from 2007 to 2009 combined with CALIOP/CPR

91 nighttime measurements, Yang et al. (2022) suggested that the dust mass loading at 4-10 km in the

92 Northern Hemisphere reaches a maximum in March-April-May. The dust concentrations in 4-6 km

93 have an opposite phase with the wind speed over Africa and West Asia. Despite the great coverage of

94 satellite data, remote sensing techniques have considerable uncertainty in retrieving the dust vertical

95   distribution. In this study, we constrain the simulations with the airborne in-situ measurement of dust

96   vertical distribution from the Atmospheric Tomography Mission (ATom) from 2016 to 2018 (Froyd et

97   al., 2022; Wofsy et al., 2018). These data are primarily taken over the oceans, well away from dust

98   source regions.

99   Climate models are used to quantify the budget, emission, deposition, and climate implications of

100   dust aerosols. However, climate models have considerable uncertainty in their parameterizations of the

101   emissions, horizontal and vertical transport, and wet/dry deposition processes of dust aerosols

102   (Huneeus et al., 2011; Kim et al., 2014; Pu and Ginoux, 2018; Boucher et al., 2013). Limited in-situ

103   observations of dust properties on the global scale introduce considerable uncertainty to the simulated

104   dust cycle (e.g., Kim et al., 2014; Wu et al., 2020). For instance, the simulated global dust mass burden

105   varies by a factor of four among the dust models reported in Zender et al. (2004). Huneeus et al. (2011)

106   found large differences in the simulated dust lifetime among AeroCom models, mostly between 1.6 and

107   7.1 days. In addition, the simulated annual emissions of dust ranged between 500 and 4400 Tg yr−1

108   among the 15 GCMs. Shindell et al. (2013) showed that simulated dust AOD varies by more than a

109   factor of two among ten climate models in the Atmospheric Chemistry and Climate Model

110   Intercomparison Project (ACCMIP). Pu and Ginoux (2018) found that the Coupled Model

111   Intercomparison Project Phase 5 (CMIP5) models failed to capture interannual variation in the optical

112   depth of dust (DOD). Yu et al. (2010) showed that the modeled dust extinction of GOCART exceeded

113   CALIOP's measurements by more than a factor of two from the middle to the upper troposphere over

114   the northwestern Pacific.

115   We use a sectional aerosol model coupled with a climate model to study the global distribution of

116   dust, with a focus on vertical distribution. We compare the simulated dust abundance in the lower and

117   upper troposphere with satellite and in-situ measurements from a pole-to-pole airborne field campaign

118   (Froyd et al., 2022) and the global surface dust measurement network. Then we use the constrained

119   model to simulate the spatiotemporal distribution of dust coming from the Sahara, Middle East, and

120   East Asia. Finally, we estimate dust source attributions during the Asian summer monsoon from the

121   three source regions.

2   Methods

2.1 CESM1/CARMA model

We use a sectional aerosol microphysics model, the Community Aerosol and Radiation Model for

Atmospheres (CARMA) (Yu et al., 2015b; Yu et al., 2019; Bardeen et al., 2008; Toon et al., 1988)

coupled with the NSF/DOE Community Earth System Model (CESM) to simulate the global

distribution of dust between 2014 and 2019. The model simulations are conducted at a horizontal

resolution of 1.9°×2.5° and with a time step of 30 min. The model has 56 hybrid levels from the surface

up to about 45 km, with a vertical resolution of about 1 km near the tropopause. The meteorological

fields were nudged to Goddard Earth Observing System (GEOS5) reanalysis data.

CESM1/CARMA includes two groups of particles. The first group is liquid sulfuric acid droplets

that form from gas phase nucleation and span a diameter range from 0.2 nm to 2.6 μm. The second

group is an internal mixture of primary emitted organics, secondary organics, dust, sea salt, black

carbon, and condensed sulfate (Yu et al., 2015b). The mixed particles are resolved with 20 discrete size

bins with diameters ranging from 100 nm to 17 μm in the model. The aerosol optical properties in

CESM1/CARMA are estimated using a Mie scattering code, with inputs based on particle size, relative

humidity, and aerosol composition (Yu et al., 2015b). We assume that dust has a density of 2.65 g/cm^3

and use mid-visible refractive indices of 1.53-0.006i independent of the dust source region, even

though these properties vary with dust source in reality.

2.2 Dust emission parameterization

Mineral dust emission is simulated as a saltation-sandblasting process, which can be explained by the

wind erosion theory. The process is driven by surface stress, which is usually expressed as friction wind

velocity (Su and Toon, 2009). When the frictional wind speed exceeds a certain threshold, the force of

the wind will overcome the gravitational force of the sand grains and the cohesive forces between

particles, and sand-sized particles will saltate. When they impact the surface dust particles will be

lofted into the air (Marticorena and Bergametti, 1995). The wind-driven emission of dust aerosols in

CESM1/CARMA is provided by Su and Toon (2009) and Yu et al. (2015b). The total emission flux is

parameterized as:

$$F_{total} = C \times S_e \times (u - u_t) \times u^2,$$

where F_{total} is the particle size dependent flux of dust; C is an arbitrary constant that depends on

151   the spatial resolution of the climate model among other factors and is set to $0.6\ \mu g\ s^2 m^{-5}$; u is the 10-

152   m wind speed, which is parameterized by the surface friction velocity (u^*) and the 10-m drag

153   coefficient (C_d) so that under neutral conditions $u = \frac{u^*}{\sqrt{C_d}}$; and u_t is the threshold wind speed, which

154   depends on the particle size (Su and Toon, 2009; Marticorena and Bergametti, 1995). Details on u^*, u_t ,

155   and C_d can be found in Yu et al. (2015b). S_e is the dust erodibility factor, which denotes the efficiency

156   of dust lifting and derived from the TOMS aerosol index reported by Ginoux et al. (2001).

157   Following Prospero and Bonatti (1969), the model assumes that 90% of the dust emission mass

158   flux is distributed in silt bins with diameter ranges from 2.6 to 17.4 µm, and the remaining 10% is in

159   clay bins with diameter ranges from 0.1 to 2 µm (Yu et al., 2015b). In the present study, we adjust the

160   relative mass fractions in clay and silt bins to match the data reported by Adebiyi and Kok (2020) and

161   discussed in section 3.1 below.

162   **2.3 Convective transport parameterization**

163   CESM1/CARMA considers the secondary activation of particles, including dust, above the cloud base

164   in convective plumes (Froyd et al., 2022; Yu et al., 2019). Previous studies have found that climate

165   models that fail to consider secondary activation above the cloud base overestimate the abundance of

166   primary particles like sea salt and black carbon in the upper troposphere by orders of magnitude (Yu et

167   al., 2019; Murphy et al., 2021). A comparison with global airborne measurements of dust suggests that

168   dust is also subject to secondary activation above the cloud base and subsequent in-cloud removal

169   (Froyd et al., 2022). For below-cloud scavenging, we assume that dust's solubility is 0.2 which is lower

170   than sea salt's solubility of 1.0. For convective removal, we treat dust's removal efficiency the same as

171   other aerosol types. Details of the parameterizations can be found in Wang et al. (2013), Grell and

172   Freitas (2014), and the supplement of Yu et al. (2019).

173   **2.4 ATom airborne field campaign**

174   The Atmospheric Tomography Mission (ATom) was an airborne field campaign with in-situ

175   measurements of atmospheric composition in the remote troposphere from about 0.18 to 12 km in

176   altitude in the Pacific and Atlantic basins, spanning from ~82°N to ~86°S latitude (Spanu et al., 2020;

177   Wofsy et al., 2018). It consisted of 48 science flights by the NASA DC-8 aircraft with 548 vertical

178   profiles during four flight series covering roughly the same loop (Bourgeois et al., 2020). A

179   comprehensive set of aerosol measurement data including mineral dust was collected from July 2016 to

180   May 2018.

181   In this study we compare the simulations with measured dust concentrations during the ATom

182   mission from 2016 to 2018. Dust concentration data are based on data from the National Oceanic and

183   Atmospheric Administration (NOAA) Particle Analysis by Laser Mass Spectrometry (PALMS)

184   instrument (Froyd et al., 2019; Brock et al., 2019; Murphy et al., 2003). The PALMS instrument

185   measures the chemical composition of individual ambient particles from about 0.15 to 5 μm in diameter

186   by evaporating individual particles and then using a time of flight mass spectrometer to analyze ions

187   (Murphy et al., 2006). Dust and other particle types are classified using spectral signatures. Dust mass

188   concentrations are then determined by combining the PALMS classifications with absolute particle

189   concentrations from independent optical particle counters (Froyd et al., 2019; Froyd et al., 2022).

190   **2.5 Surface measurement networks**

191   Huneeus et al. (2011) summarize dust measurements at the surface around the globe including those

192   from cruises and long-term surface measurements compiled by Mahowald et al. (2009) and the

193   University of Miami network Prospero, 1989; Arimoto et al., 1996). Data compiled by Mahowald et al.,

194   (2009) contain the data set of cruises and long term measuring stations with monthly averaged surface

195   dust concentrations. Cruises measured iron (Fe) and converted to dust by assuming a 3.5% Fe in dust.

196   The iron content in dust varies according to the source regions and this value is the average iron

197   content of the Earth's crust (Mahowald et al., 2005). Long-term observations by the University of

198   Miami include Pacific, Atlantic, and Antarctic Ocean sites globally and measure the mass concentration

199   of dust with diameter less than 40 μm (Prospero, 1989, 1996; Arimoto et al., 1996).

200   **3 Model validation**

201   **3.1 Dust size distribution and emission**

202   Based on global measurements of atmospheric dust size distributions, Adebiyi and Kok (2020) found

203   that the global models in AeroCom (Aerosol Comparison between Observations and Models project)

204   underestimate the coarse dust mass load in the atmosphere by a factor of four and overestimate the fine

205   dust mass load by 1-3 orders of magnitude. Figure 1 shows that CESM1/CARMA Yu et al. (2015b)

206   generally reproduces the measured dust size distribution with diameter less than 1 μm or greater than 3

207 μm within the variabilities of the data. However, the CESM1/CARMA Yu et al. (2015b)

208 underestimates the dust in the size range between 1 and 3 μm by one order of magnitude (red dashed

209 line). In this study, we simply adjust the mass fraction of the emitted dust in the silt bins with diameter

210 less than 2 μm from 90% to 94%. The global dust size distribution simulated in the modified model

211 (CESM-CARMA solid red line in Fig.1) agrees better with measurements from Adebiyi and Kok

212 (2020) (Figure 1).
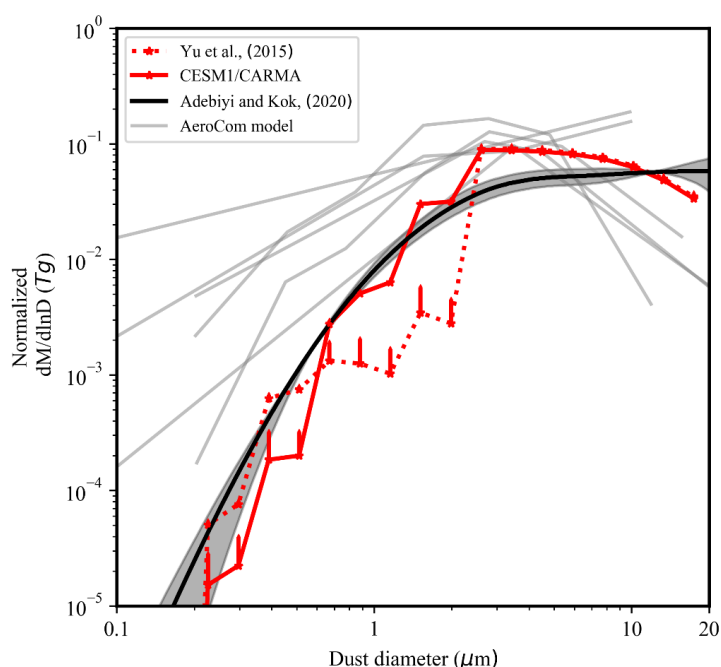
213

214 **Figure 1.** Comparison of the simulated and measured normalized global mean dust size distributions.

215 The global and annual mean dust size distribution simulated by CESM1/CARMA with the dust

216 emission parameterization described in Yu et al. (2015b) is shown by the dashed red line; the

217 simulation by CESM1/CARMA with the modified emission parameterization is shown by the solid red

218 line; temporal variabilities (1 standard deviation) from Yu et al., (2015b) and CESM1/CARMA are

219 denoted by green and cyan lines; the simulated size distribution by the AeroCom models reported in

220 Adebiyi and Kok (2020) is denoted by the gray lines; the measured dust size distribution derived from

221 the global measurements reported in Adebiyi and Kok (2020) is denoted by the solid black line; the

222 shading represent the 95% confidence interval.

223   Figure 2 shows the global annual mean emission of fine (with diameter less than 4.5 µm) and

224   coarse (with diameter greater than 4.5 µm) dust simulated by CESM1/CARMA. The simulated global

225   and annual mean mass emission of coarse dust is higher than that of fine dust by a factor of 2.8. The

226   three largest dust source regions in the world, i.e., the Sahara, Middle East, and Asia contribute ~85%

227   of total global dust emissions, and about 97% of Northern Hemisphere dust. Dust emissions from the

228   Sahara in North Africa account for ~59.7% of global emissions by mass. Middle Eastern and Asian

229   dust emissions account for ~12.5% and 13.3% of global emissions, respectively.
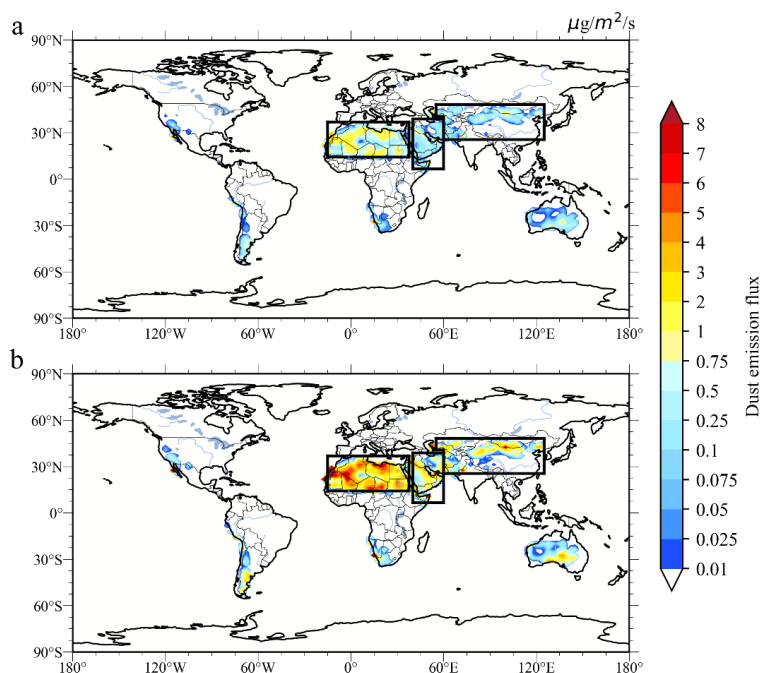
230

231   **Figure 2.** (a) Simulated annual emission flux (µg/m2/s) of dust with diameter less than 4.5 µm in

232   CESM1/CARMA averaged from Feb 2014 to Jan 2018. (b) same as (a) but for dust with diameter

233   larger than 4.5 µm. The regions of interest (Saharan, Middle Eastern, and Asian source regions) are

234   denoted by the black boxes.

235   **3.2 Comparison with dust surface measurements**

236   In Figure 3, we compare the simulated annual mean dust concentrations at the surface from 2014 to

237   2018 with the observational datasets summarized in Huneeus et al. (2011). In general, the simulated

238   dust concentrations are within one order of magnitude of observations (Figure 3b). Both the model and

239 observations show that the dust concentration in the Northern Hemisphere (NH) is about one order of

240 magnitude higher than that in the Southern Hemisphere (SH) due to higher NH dust emissions because

241 of the greater area of Northern Hemisphere deserts. Simulated dust concentrations are underestimated

242 by 13% and 57% comparing with University of Miami network and the compiled datasets from

243 Mahowald et al. (2009), respectively. Near the dust source region (e.g., downwind of the Sahara), the

244 model underestimates the measured median dust surface concentrations by 5.4%. The dust simulation

245 underestimates the averaged ship cruise measurements by 11% over remote ocean basins in the SH.

246 Higher model low biases of 72% are found in the tropical Pacific, which indicates that dust is removed

247 too efficiently amid transport from the source regions.
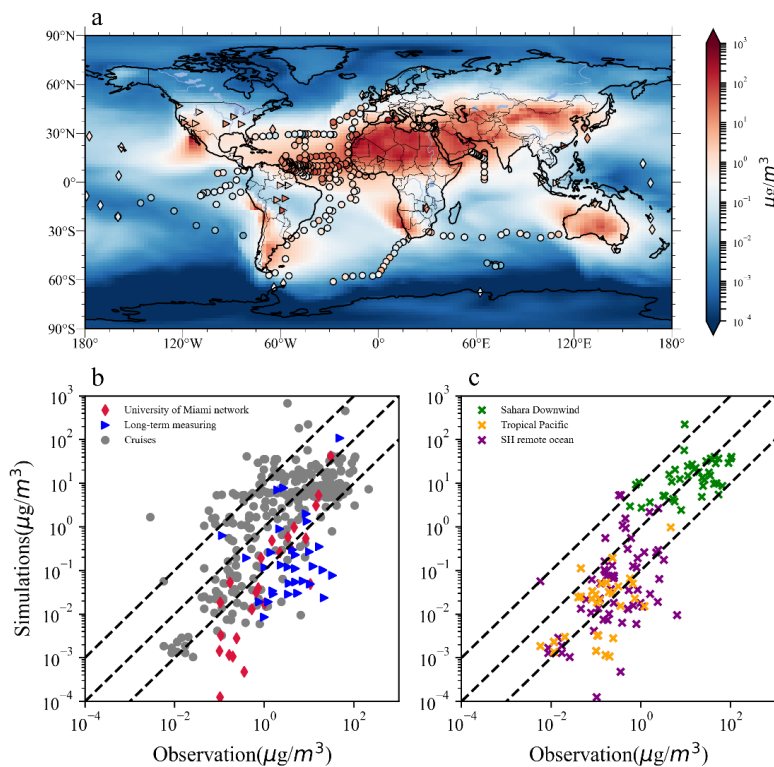
248

249 **Figure 3.** (a) Simulated global dust surface concentrations (μg/m3) averaged from 2014 to 2019 from

250 CESM1/CARMA shown in the filled contour. The summarized dust surface concentration data sets

251 from Huneeus et al. (2011) are denoted by markers of different shapes. Compiled observations

252 including those from long-term observational sites and cruise data reported in Mahowald et al. (2009)

253 are denoted by triangles and circles, respectively; measurements from the University of Miami network

254   (PROSPERO, 1989; Arimoto et al., 1996) from 1981 to 1998 are denoted by diamonds. (b)

255   Comparison of the simulated dust concentrations by CESM1/CARMA with the compiled observational

256   dataset from Mahowald et al. (2009) and University of Miami network. Gray circles and blue triangles

257   represent selected data from Mahowald et al. (2009) short-term cruises and long-term observations,

258   respectively; red diamonds represent the University of Miami network measurements. (c) Same as (b),

259   but the North African downwind area as well as the tropical Pacific basin and Southern Hemisphere

260   remote ocean are represented as green, orange, and purple stars, respectively. The 1:1, 1:10, and 10:1

261   relationships between the simulated and observed dust concentrations are denoted by the black dashed

262   lines.

263   Figure 4 compares the simulated concentrations of dust below 1 kilometer above the sea level with

264   diameter less than 4.5 μm near the surface (0-1 km above sea level) over remote ocean basins with the

265   NASA Atmospheric Tomography (ATom1) airborne field campaign (Froyd et al., 2022; Wofsy et al.,

266   2018). Both observations and the model suggest that higher dust concentrations are found in the

267   Atlantic basin downwind of the Saharan Desert and near the west coast of North America. As shown in

268   Figure 4c, the model underestimates the average dust surface concentrations observed during ATom1

269   by ~43%, with a correlation coefficient of 0.51. Except for the Southern Ocean, the modeled dust

270   concentration is within an order of magnitude of the observations in general. The model strongly

271   underestimates the observed dust concentration in the remote Southern Ocean by over one order of

272   magnitude. The underestimation of southern Pacific Ocean dust could be partly due to underestimation

273   of the emissions in SH. In addition to a possible lack of emissions, the model may generate too much

274   convection and thereby have a too efficient wet scavenging of dust aerosols.
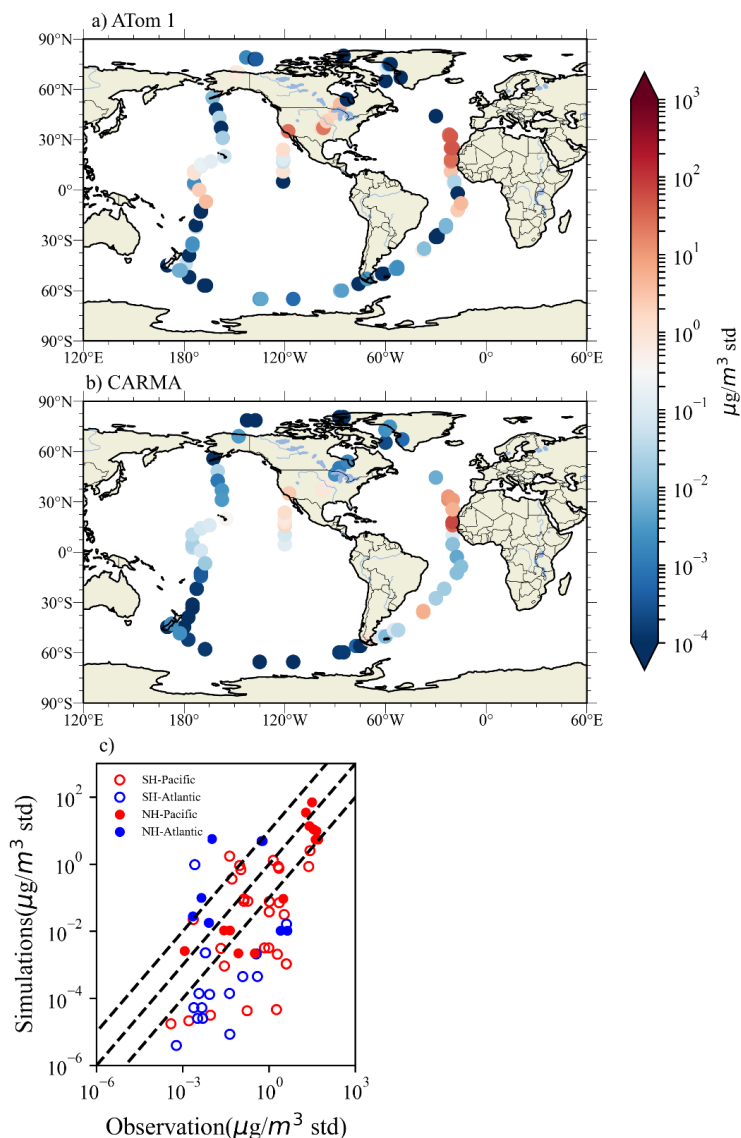
Figure 4. Comparison of the dust concentration below 1 kilometre above sea level with diameter less

than 4.5 μm simulated by CESM1/CARMA with the NASA ATom 1 airborne campaign. (a) Observed

dust surface concentration according to ATom 1; (b) same as (a), but simulations from

CESM1/CARMA. (c) Scatterplot CARMA simulation compared with ATom 1 for dust surface

concentration. Southern Pacific and Atlantic basin sites are denoted by red and blue circles,

respectively, while northern Pacific and Atlantic basin sites are denoted by red and blue points,

282   respectively. The black dashed lines in each panel denote 1:10, 1:1, and 10:1 relationships between

283   observations and simulations, respectively.

284   **3.3 Comparison with dust vertical distribution**

285   Figure 5 compares the dust vertical distribution between CESM1/CARMA and measurements by

286   PALMS during ATom1 in August 2016. The observed dust concentrations in the lower tropospheric NH

287   midlatitudes (27ºN-60ºN) and tropics (27ºS-27ºN) are about an order of magnitude higher than those in

288   the SH midlatitudes (27ºS-60ºS) due to higher surface emissions in NH (Figure 2). The tropical lower

289   tropospheric dust loading in the Atlantic basin, which is downwind of the Saharan Desert, is over one

290   order of magnitude higher than that in the Pacific Ocean. Both observations and the model show that

291   the dust concentration decreases by two to three orders of magnitude from the surface to about 200

292   hPa. The strong vertical gradient is consistent with the findings reported in Yu et al. (2019) and Froyd

293   et al. (2022), that deep convection activates the entrained dust aerosols above the cloud base and

294   subsequently removes the particles in-cloud. Maloney et al. (2022) suggests that there is a strong

295   removal of dust by ice formation through heterogeneous nucleation. The model overestimates the

296   observed dust concentration in the mid and upper troposphere possibly because our model does not

297   include the interaction. A layer of dust between 800 and 400 hPa, which the model fails to reproduce

298   over the southern Atlantic, is observed during ATom1 but not in ATom2-4 (Figure S1-S3). Figure 5

299   shows that about 52% of the simulated dust near the surface are coarse mode dust (4.5um – 17 um) and

300   the coarse dust mass fraction drops rapidly with altitude. Simulations show that 95% of the total dust

301   concentration in the upper troposphere is fine dust (with diameter less than 4.5 μm) because coarse dust

302   is subject to more efficient wet and dry deposition during long-range transport vertically or

303   horizontally.
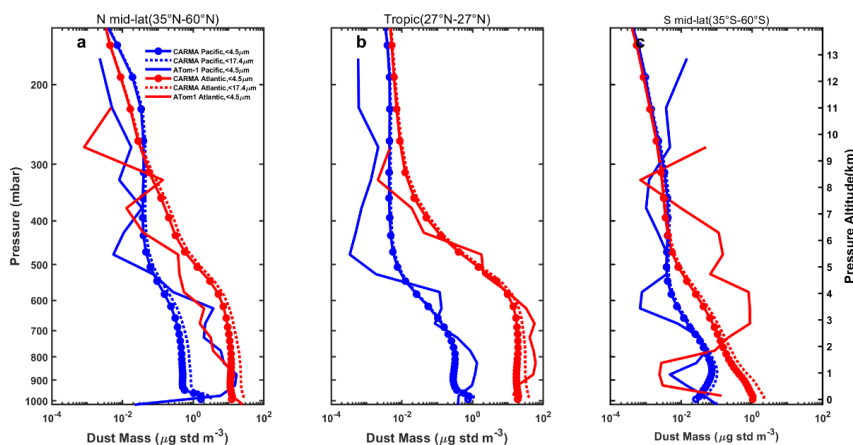
304

305 **Figure 5.** Simulated (dotted solid line) and measured (solid line) vertical profiles of the dust

306 concentrations in August 2016 during the ATom1 field campaign. The dashed lines represent the

307 simulated vertical distribution of the total dust concentration (diameter up to 17.4 μm). The profiles are

308 averaged over the Pacific Ocean (red) or Atlantic Ocean (blue) in the Northern Hemisphere

309 midlatitudes (27ºN-60ºN, panel a) and tropics (27ºS-27ºN, panel b), and in the Southern Hemisphere

310 midlatitudes (27ºS-60ºS, panel c).

311 **3.4 Comparison with AERONET in Asia and the Sahara**

312 The simulated aerosol optical depth (AOD) at 1020 nm wavelength from CESM1/CARMA is

313 compared to the measurements near dust source regions from 2014 to 2018 for most of the Aerosol

314 Robotic Network (AERONET) sites (Figure 6a). On average, the model underestimates the averaged

315 AOD of all AERONET sites by ~10%, with ~21% underestimation in the Sahara and Middle East

316 where dust dominates the AOD (Chin et al., 2009). Consistent with the dust emission distribution

317 shown in Figure 2, the simulated and observed AOD near the dust source regions in the tropics and NH

318 (e.g., Sahara, Middle East, and Asia) is significantly higher than that near SH deserts (e.g., central

319 Australia). Dust from the source regions in NH and tropical deserts is transported downwind into the

320 Pacific and Atlantic Ocean basins.
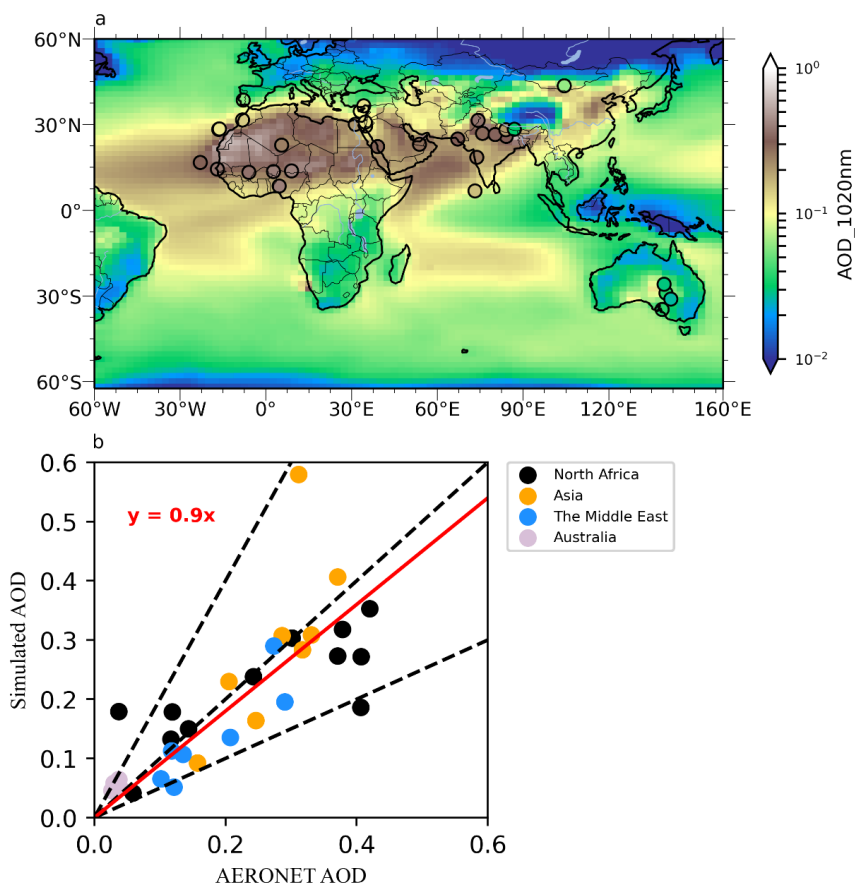
Figure 6. (a) Annual mean AOD at 1020 nm wavelength from 2014 to 2018 simulated by

CESM1/CARMA, denoted by the color-filled contours. The measured AOD from 33 AERONET

ground sites is denoted by the color-coded circles. (b) Comparison of the simulated annual mean AOD

at 1020 nm wavelength with measurements from 2014 to 2018 for the most of the AERONET sites

except for Australian sites. Due to the limited data availability in Australian AERONET sites, the

multiyear annual mean AOD from year 1998 to 2022 are used. North Africa, the Middle East, Asia, and

Australia are represented as black, green, blue, and pink circles, respectively. The solid red line denotes

the best fit. The dashed black lines represent 1:2, 1:1, and 2:1 relationships between the observations

and simulations.

4 Global distributions of Saharan, Middle Eastern, and Asian dust

4.1 Surface distribution of dust

Figure 7 shows the simulated annual mean surface concentrations of Saharan, Middle Eastern, and

Asian dust and their relative contributions to the simulated total dust from 2014 to 2018. In general, the

simulated maximum concentrations are located near the source regions. The dust concentrations

decrease dramatically by about two to three orders of magnitude from the source to remote regions due

to efficient dry and wet scavenging. Limited dust is transported across the equator from NH to SH

midlatitudes at the surface level. The simulated NH dust can travel to SH once convection lifts the dust

into the upper troposphere and lower stratosphere (Section 4.2).
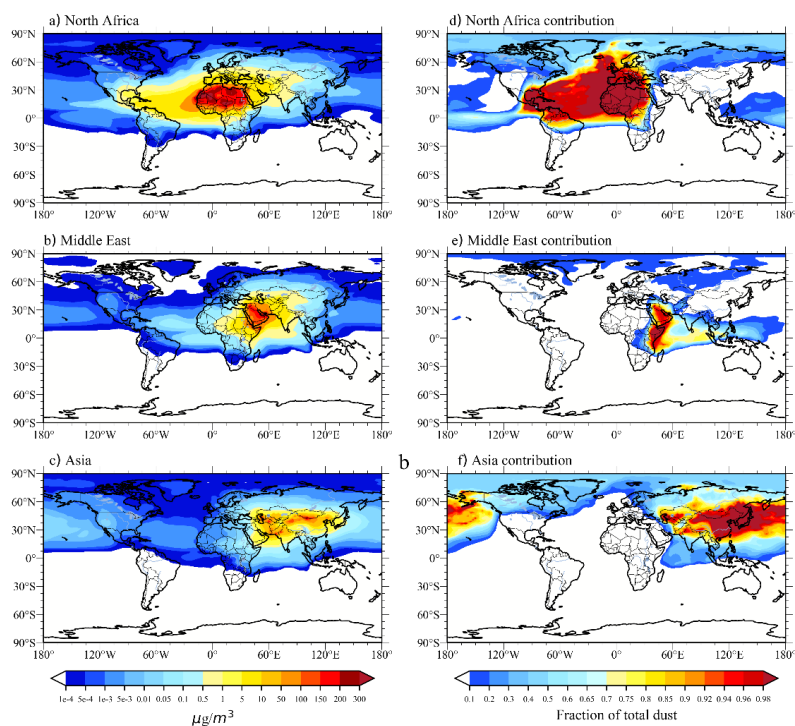
Figure 7. Simulated global spatial distribution of annual mean surface dust mass concentrations and

the fractional contribution of each source. Simulations are averaged from 2014 to 2018. Left panels

represent each source's concentration of dust. Right panels represent each source's contribution to total

dust.

Saharan dust dominates the surface dust concentrations in the Western Hemisphere including the

346   North Atlantic basin, Europe, Caribbean, and eastern North America. The model suggests that

347   simulated Saharan dust concentrations drop by three orders of magnitude during transport from North

348   Africa to 60 °N and peaks in the Caribbean. The modeled shape and direction of the transported dust

349   plume is similar to the simulations of Colarco et al. (2003). The simulated annual mean dust

350   concentration in Asia is about 24% of that in the Saharan Desert, which Su and Toon (2011) attribute to

351   Asia having a much smaller area of dust sources than the Sahara. Asian dust dominates in the Eastern

352   Hemisphere including the North Pacific basin, Russia, and some can be transported to Alaska and

353   Canada. Previous studies have indicated that dust from the Gobi Desert region entrained in a surface

354   cyclone arrives in the western U.S. boundary layer via cross-Pacific transport (Arimoto et al., 1996).

355   With CARMA we show that although some Asian dust can be transported to the western U.S. across

356   the Pacific basin (Figure 7), its relative mass contribution to the total dust concentration in the Western

357   U.S. is about 1% on the annual basis (Figure 3). Simulated dust in the boundary layer is mostly

358   removed by wet and dry deposition during the cross-Pacific transport, while lifted Asian dust can be

359   transported more efficiently across the Pacific basin and accounts for about 50% of the dust loading in

360   the middle troposphere above the western U.S. (Figure S4). The Pacific Dust Experiment (PACDEX)

361   shows that the coarse mode Asian dust is rapidly removed amid the remote transport, while the fine

362   mode dust less than 2.5 um in diameter is entrained into the upper air and transported across the Pacific

363   Basin by the upper tropospheric westerly jets (Stith et al., 2009). Consistent with PACDEX, our model

364   shows that 92% of Asian dust mass that transported 10 km above U.S. are less than 2.5 um in diameter

365   (not shown). Middle Eastern dust contributes significantly to surface dust loading over the Indian

366   Ocean, eastern edge of Africa, southern India, and Southeast Asia. The simulated latitudinal transport

367   of Middle Eastern dust is limited (Figure S4). Our model suggests that the contribution of Saharan and

368   Asian dust to the surface dust in the Arctic is similar. Note that the current model fails to consider high-

369   latitude dust sources in Siberia and Alaska, which are believed to be the major contributors to Arctic

370   dust (Lambert et al., 2015; Zwaaftink et al., 2016).

4.2 Vertical distribution of dust

372   Figure 8 compares the simulated vertical distributions of Saharan, Middle Eastern, and Asian dust in

373   the lower, middle, and upper troposphere averaged from 2014 to 2018. Simulated global dust

374   concentrations drop by one order of magnitude from the surface to about 600 hPa and by four orders of

375   magnitude from the surface to 160 hPa. The rapid decline of dust mass concentration is due mostly to

376   deposition and subgrid-scale convective removal above the cloud base (Yu et al., 2019; Froyd et al.,

377   2022). However, Maloney et al. (2022) show that heterogenous nucleation of ice on dust, followed by

378   sedimentation also contributes to loss of dust from the mid and upper troposphere. Model results show

379   that the dust from the Sahara, Middle East, and Asia accounts for ~61.7%, 12.9%, and 13.9% of global

380   annual mean surface dust concentration, respectively. In the NH midlatitudes, the relative contribution

381   of Asian dust increases with altitude and becomes dominant in the upper troposphere. Asian dust

382   contributes ~60.9% of the dust at pressures from 266 hPa to 160 hPa. Asian dust is mostly lifted in the

383   spring by mid-latitude frontal systems (Caffrey et al., 2018). This higher relative contribution of Asian

384   dust in the upper troposphere of the NH midlatitudes and tropics suggests that Asian dust is lifted more

385   efficiently than Saharan dust. Asian dust is mostly lifted in mid-latitude springtime weather systems

386   that are efficient at transporting dust aloft. Saharan dust is lifted in tropical systems that are less

387   efficient at transporting dust to high altitudes since there is widespread descending air at the latitudes of

388   the Saharan Desert, which is in the descending branch of the Hadley circulation (Su and Toon, 2011).

389   The upward transport of Saharan dust is restricted due to infrequent deep convection over the Saharan

390   Desert (Froyd et al., 2022). Frequent convective activity and cold frontal systems (Kawai et al., 2018,

391   2015; Hara et al., 2009) transport Asian dust upward to higher altitudes. Figures 8d-8e show that the

392   upper tropospheric dust concentration in the NH midlatitudes is about one order of magnitude higher

393   than that in the tropics.
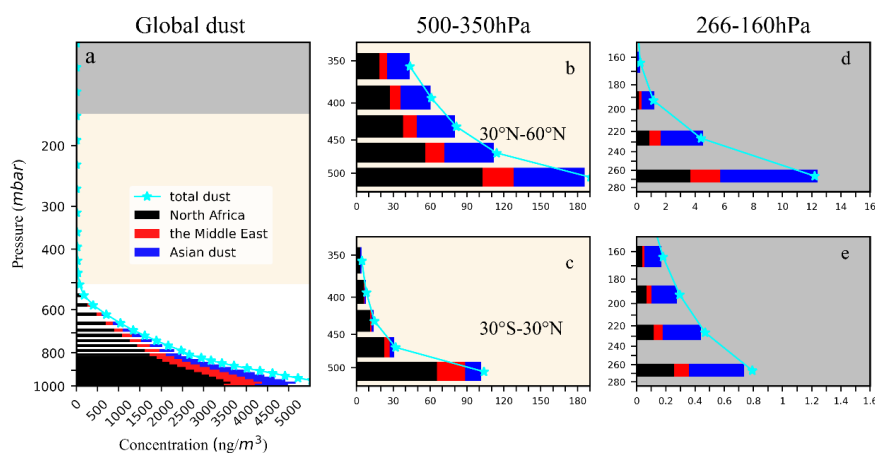
394

395   **Figure 8.** (a) Simulated vertical profiles of average dust concentration for 2014 to 2018 from each

396   desert emission zone; green bars denote Saharan dust, red bars denote Middle Eastern dust, and blue

397   bars denote Asian dust. (b-d) Same as Figure 8a but averaged for Northern Hemisphere midlatitudes

398   (30°N-60°N) and tropics (30°S-30°N) from 500 to 350 hPa. (d-e) Same as Figure 8b-8c but for

399   pressure levels from 266 to 160 hPa.

400   Figure 9 shows the vertical distribution of the annual mean dust fractional contributions from the

401   three dust source regions. The Sahara dominates the tropical dust budget from the surface to the upper

402   troposphere and accounts about 50% of dust in the troposphere of the NH mid-high latitudes. The

403   model shows that limited Saharan dust is transported into the stratosphere. In contrast, Asian dust

404   contributes less than Saharan dust in the troposphere except for the midlatitudes where the sources are

405   located. Asian dust contributes more than 40% of the dust in the global UTLS, with the peak in the NH

406   midlatitude UTLS having a mass fraction of more than 60%. Once the Asian dust is lifted high enough

407   into the stratosphere, some can be transported to the SH UTLS. Our model suggests that Asian dust

408   might be the dominant source of ice nucleating particles in the global UTLS. The simulations show that

409   the fractional contribution of Saharan and Asian dust is comparable in the lower and middle

410   troposphere of the Arctic.
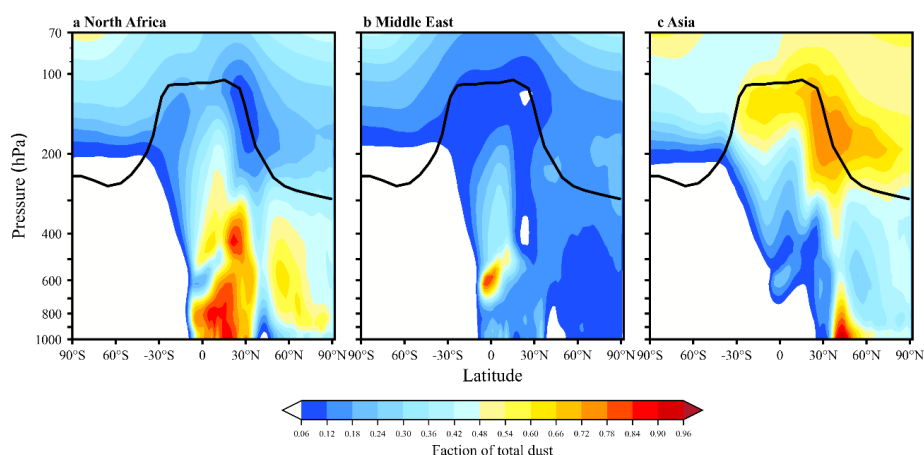
411

412   **Figure 9.** Simulation of each dust source's fractional contribution to annual average total dust as a

413   function of altitude (left axis) and latitude (bottom axis). Shading indicates dust concentrations, and the

414   black line in each figure denotes the annually averaged simulated tropopause height.

5 Dust attribution in the Asian summer monsoon region

A layer of aerosols in the UTLS of the ASM is revealed by satellites (Thomason and Vernier, 2013; Vernier et al., 2015; Vernier et al., 2011) and balloon-borne optical particle counters (Vernier et al., 2018; Yu et al., 2017). In the meantime, a high occurrence of cirrus clouds is found by satellites (Sassen et al., 2008; Nazaryan et al., 2008), and dust particles might play an important role in cirrus formation in the ASM region. Recent airborne in-situ measurements suggest that the ASM tropopause aerosol layer is composed of mostly sulfate, organics, and nitrate (Hopfner et al., 2019; Appel et al., 2022). The budget of dust particles near the tropopause (~100 hPa) and at cirrus altitudes (e.g., 500-200 hPa) remains unquantified.

Figure 10 illustrates the simulated June-July-August (JJA) dust concentrations at 100 hPa averaged from 2014 to 2018. A peak of dust is simulated in the ASM region associated with the anticyclonic air flow similar to sulfate and organics. However, the dust abundance is extremely limited compared with sulfate and organics. The simulated mass fraction of aerosol contributed by dust is ~3% at 200 hPa and 0.04% at 100 hPa inside the ASM. As expected, Asian dust dominates the dust budget in the ASM region, with a relative contribution 1-2 orders of magnitude higher than Saharan and Middle Eastern dust. There is limited Saharan and Middle Eastern dust transport to the ASM region by the strong upper tropospheric westerlies (Tanaka et al., 2005; Prasad and Singh, 2007). Note that the dust concentration simulated by CESM1/CARMA at 100 hPa in the ASM region is about 9×10^{-5} µg/m^3, which is about 3 orders of magnitude smaller than the values simulated by the CESM-MAM7 model reported by Bossolasco et al. (2021). Such low values of dust concentration are due to inclusion of secondary activation of dust above the cloud base in the convective transport scheme revised by Yu et al. (2019). Failure to include this removal will lead to large overestimates of dust aloft.
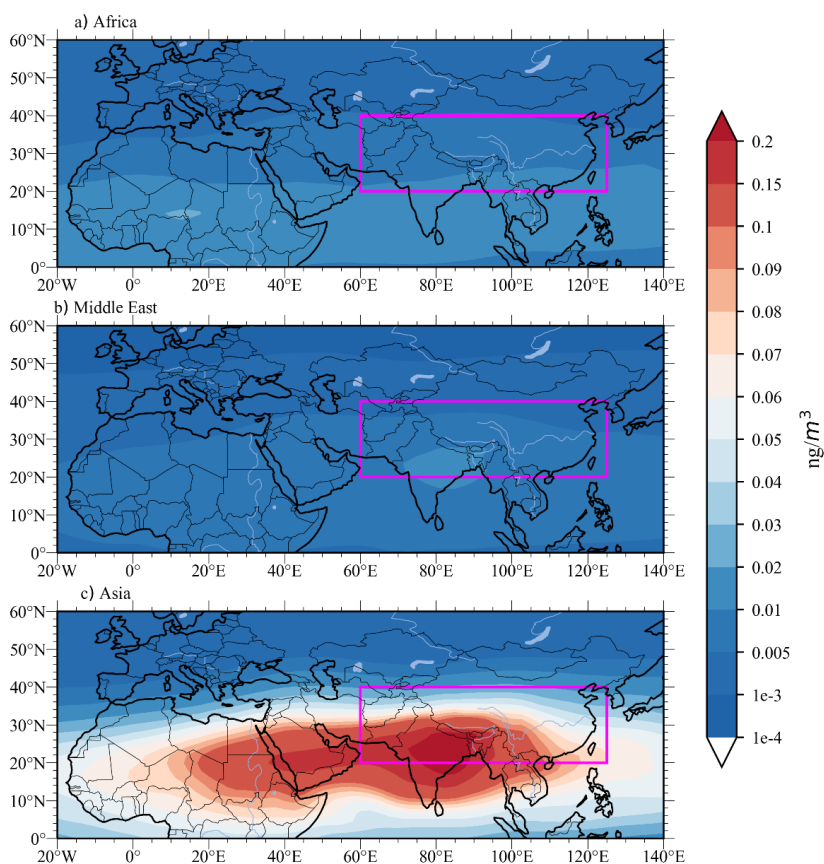
Figure 10. Simulated mass concentrations of Saharan, Middle East and Asian dust at 100 hPa (left)

averaged in June-July-August (JJA) from year 2014 to 2018. Purple boxes denote the Asian Summer

Monsoon region.

6 Summary

This study uses a sectional aerosol model coupled with a climate model, CESM1/CARMA, to simulate

the global distribution of dust, 85% over which comes from Asian, Middle Eastern, and Saharan

sources. Compared with measurements reported in Adebiyi and Kok (2020), the model of Yu et al.

(2015b) underestimates the observed dust in the size range between 1 and 3 μm by one order of

magnitude. We modified the size distribution of the dust emission, and the improved model is within

the error bars of measurements summarized by Adebiyi and Kok (2020). Both observations and the

448   simulations suggest that the dust mass size distribution increases by about 4 orders of magnitude from

449   0.1 μm to 2 μm, reaches its highest values around 2-3 micrometers in diameter and remains fairly

450   constant for larger sizes up to 20 μm diameter. We compared the simulated dust distributions with

451   multiple observational datasets including surface and airborne in-situ measurements over remote

452   regions and aerosol optical depth measurements near the dust source regions. CESM1/CARMA

453   reproduces the annual mean dust surface concentrations around the globe within one order of

454   magnitude of the observations summarized in Huneeus et al. (2011). The global vertical distributions of

455   dust measured by PALMS during the NASA ATom field campaign are used to constrain the model.

456   Both the model and PALMS measurements suggest that dust mass concentrations over remote ocean

457   basins drop by two to three orders of magnitude from the surface to the upper troposphere (200 hPa).

458   Simulations show that about 52% of dust near the surface are coarse, while 95% of the total dust

459   concentration in the upper troposphere is fine dust (with diameter less than 4.5 μm). The rapid decline

460   of dust aerosols with altitude is associated with the efficient in-cloud convective removal of dust

461   aerosols (Froyd et al., 2022; Yu et al., 2019). However, in situ cirrus formation can also lead to

462   downward transport of dust (Maloney et al., 2022). In addition, both the model and PALMS

463   measurements suggest that dust concentrations in the lower troposphere of the NH midlatitudes (27ºN-

464   60ºN) and tropics (27ºS-27ºN) are about an order of magnitude higher than that in the SH midlatitudes

465   (27ºS-60ºS). The model captures ~90% of the annual mean column aerosol optical depth measured by

466   33 AERONET stations near the dust source regions.

467   Our simulations suggest that the annual mean dust emissions from the Sahara, Middle East, and

468   Asia account for ~59.7%, 12.5%, and 13.3% of global annual mean dust emissions, respectively. Dust

469   emitted from the Sahara is transported toward Europe, but mostly to the Western Hemisphere including

470   the North Atlantic basin, and eastern North America. Asian dust dominates the Eastern Hemisphere

471   including the North Pacific basin, Russia, and some can be transported to Alaska and Canada. Middle

472   Eastern dust contributes significantly to the surface dust over the Indian Ocean, the eastern edge of

473   Africa, southern India, and Southeast Asia. Although Saharan dust dominates global dust mass loading

474   at the surface, the relative contribution of Asian dust increases with altitude and becomes dominant in

475   the upper troposphere of the northern hemisphere. Once the Asian dust is lifted high enough into the

476   stratosphere, some can be transported to the SH UTLS. Asian dust might be the dominant source of ice

477   nucleating particles in the global UTLS. Asian dust contributes ~60.9% of the dust mass at pressure

478   levels from 266 hPa to 160 hPa. The increasing fractional contribution of Asian dust is due to efficient

479   vertical transport in midlatitude weather systems, while tropical weather systems are not as efficient

480   due to subsiding motion in the descending branch of the Hadley circulation and convective activity

481   over the Sahara is relatively infrequent (Froyd et al., 2022). Asian dust dominates the dust budget in the

482   global upper troposphere during the summer months, with the peak fractional contribution in the ASM

483   region, which is about 1-2 orders of magnitude higher than that of Saharan and Middle Eastern dust.

484   The model suggests that the dust forms a local maximum in the ASM anticyclone as well as organics

485   and sulfate. However, the simulated dust mass concentration is only ~0.04% of the total aerosols in the

486   Asian Tropopause Aerosol Layer (ATAL). Constrained by the state-of-the-art measurements of dust at

487   the global scale, our model highlights the significant contribution of Asian dust to the global upper

488   troposphere where cirrus clouds may form heterogeneously.

489   *Data availability.* Dust surface measurements data are reported in Huneeus et al. (2011) and can be

490   found at https://aerocom-classic.met.no/DATA/download/DUST_BENCHMARK_HUNEEUS2011/;

491   NASA ATom data are available at https://espo.nasa.gov/atom/content/ATom; AERONET data can be

492   found http://aeronet.gsfc.nasa.gov/.

493

494   *Author contributions.* P.Y. designed the research and ran CESM1/CARMA model. S.L. analyzed the

495   model output, observational datasets and wrote the paper. L.Z, D.M.M, K.D.F and O.B.T provided

496   effective and constructive comments on the study. K.D.F and D.M.M provided the PLAMS datasets.

497   All authors edited the paper.

498

499   *Competing interests.* The authors declare no competing interests.

500

501   *Acknowledgements.* This work has been supported by the second Tibetan Plateau Scientific Expedition

502   and Research Program (2019QZKK0604); L.Z. is supported by Guangdong Innovative and

503   Entrepreneurial Research Team Program (2019ZT08G669); S.L. and P.Y. are partly supported by

504   National Natural Science Foundation of China (42175089, 42121004). OBT was supported by NSF

505   Award 1853932. Participation of PALMS in the ATom mission was supported by NOAA climate

506   funding and NASA award NNH15AB12I. We thank Charles A. Brock at NOAA for providing the

507   NASA ATom total aerosol size distribution data. The CESM project is supported by the National

508   Science Foundation and the Office of Science (BER) of the U.S. Department of Energy. We

509   acknowledge high-performance computing platform of Jinan University.

510

511 **References**

512 Adebiyi, A. A. and Kok, J. F.: Climate models miss most of the coarse dust in the atmosphere, Sci. Adv.,
513   6, 10.1126/sciadv.aaz9507, 2020.

514 d'Almeida, G. A.: A model for Saharan dust transport, J. Appl. Meteorol. Climatol., 25, 903–916, 1986.

515 Andreae, M. O.: Climatic effects of changing atmospheric aerosol levels, World Surv. Climatol., 16, 347–
516   398, 1995.

517 Andreae, M. O., Charlson, R. J., Bruynseels, F., Storms, H., Van Grieken, R., and Maenhaut, W.: Internal
518   mixture of sea salt, silicates, and excess sulfate in marine aerosols, Science, 232, 1620–1623, 1986.

519 Appel, O., Köllner, F., Dragoneas, A., Hünig, A., Molleker, S., Schlager, H., Mahnke, C., Weigel, R.,
520   Port, M., and Schulz, C.: Chemical analysis of the Asian Tropopause Aerosol Layer (ATAL) with
521   emphasis on secondary aerosol particles using aircraft based in situ aerosol mass spectrometry, Atmos.
522   Chem. Phys. Discuss., 1–37, 2022.

523 Arimoto, R., Duce, R. A., Savoie, D. L., Prospero, J. M., Talbot, R., Cullen, J. D., Tomza, U., Lewis, N.
524   F., and Ray, B. J.: Relationships among aerosol constituents from Asia and the North Pacific during
525   PEM-West A, J. Geophys. Res. Atmospheres, 101, 2011–2023, https://doi.org/10.1029/95JD01071,
526   1996.

527 Balkanski, Y., Schulz, M., Claquin, T., and Guibert, S.: Reevaluation of Mineral aerosol radiative forcings
528   suggests a better agreement with satellite and AERONET data, Atmos. Chem. Phys., 7, 81-95,
529   10.5194/acp-7-81-2007, 2007.

530 Bardeen, C., Toon, O., Jensen, E., Marsh, D., and Harvey, V.: Numerical simulations of the three-
531   dimensional distribution of meteoric dust in the mesosphere and upper stratosphere, Journal of
532   Geophysical Research: Atmospheres, 113, 2008.

533 Bossolasco, A., Jegou, F., Sellitto, P., Berthet, G., Kloss, C., and Legras, B.: Global modeling studies of
534   composition and decadal trends of the Asian Tropopause Aerosol Layer, Atmos. Chem. Phys., 21,
535   2745-2764, doi: 10.5194/acp-21-2745-2021, 2021.

536 Boucher, O., Randall, D., Artaxo, P., Bretherton, C., Feingold, G., Forster, P., Kerminen, V., Kondo, Y.,
537   Liao, H., and Lohmann, o, U.: Climate change 2013: the physical science basis, Clouds Aerosols
538   Contrib. Work. Group 5th Assess. Rep. Intergov. Panel Clim. Change Camb. Univ. Press Camb. U. K.
539   N. Y. NY USA, 2013.

540 Bourgeois, I., Peischl, J., Thompson, C. R., Aikin, K. C., Campos, T., Clark, H., Commane, R., Daube,
541   B., Diskin, G. W., Elkins, J. W., Gao, R.-S., Gaudel, A., Hintsa, E. J., Johnson, B. J., Kivi, R., McKain,
542   K., Moore, F. L., Parrish, D. D., Querel, R., Ray, E., Sánchez, R., Sweeney, C., Tarasick, D. W.,
543   Thompson, A. M., Thouret, V., Witte, J. C., Wofsy, S. C., and Ryerson, T. B.: Global-scale distribution
544   of ozone in the remote troposphere from the ATom and HIPPO airborne field missions, Atmos. Chem.
545   Phys., 20, 10611–10635, doi: 10.5194/acp-20-10611-2020, 2020.

546 Bourgeois, Q., Ekman, A. M. L., and Krejci, R.: Aerosol transport over the Andes from the Amazon Basin
547   to the remote Pacific Ocean: A multiyear CALIOP assessment, J. Geophys. Res. Atmos., 120, 8411-
548   8425, doi: 10.1002/2015jd023254, 2015.

549 Brock, C. A., Williamson, C., Kupc, A., Froyd, K. D., Erdesz, F., Wagner, N., Richardson, M., Schwarz,
550   J. P., Gao, R. S., Katich, J. M., Campuzano-Jost, P., Nault, B. A., Schroder, J. C., Jimenez, J. L.,
551   Weinzierl, B., Dollner, M., Bui, T., and Murphy, D. M.: Aerosol size distributions during the
552   Atmospheric Tomography Mission (ATom): methods, uncertainties, and data products, Atmos. Meas.
553   Tech., 12, 3081-3099, doi: 10.5194/amt-12-3081-2019, 2019.

554 Caffrey, P. F., Fromm, M. D., and Kablick, G. P.: WRF-Chem Simulation of an East Asian Dust-Infused

555  Baroclinic Storm (DIBS), J. Geophys. Res. Atmos., 123, 6880-6895, 10.1029/2017jd027848, 2018.

556 Chepil, W. and Woodruff, N.: Sedimentary characteristics of dust storms; Part II, Visibility and dust
557  concentration, Am. J. Sci., 255, 104–114, 1957.

558 Chin, M., Diehl, T., Dubovik, O., Eck, T. F., Holben, B. N., Sinyuk, A., and Streets, D. G.: Light
559  absorption by pollution, dust, and biomass burning aerosols: a global model study and evaluation with
560  AERONET measurements, Ann. Geophys., 27, 3439-3464, doi: 10.5194/angeo-27-3439-2009, 2009.

561 Colarco P R, Toon O B, Reid J S, et al. Saharan dust transport to the Caribbean during PRIDE: 2.
562  Transport, vertical profiles, and deposition in simulations of in situ and remote sensing observations[J].
563  J. Geophys. Res. Atmos., 108, doi: 10.1029/2002JD002659, 2003.

564 Cziczo, D. J., Froyd, K. D., Hoose, C., Jensen, E. J., Diao, M. H., Zondlo, M. A., Smith, J. B., Twohy, C.
565  H., and Murphy, D. M.: Clarifying the Dominant Sources and Mechanisms of Cirrus Cloud Formation,
566  Science, 340, 1320-1324, doi: 10.1126/science.1234145, 2013.

567 Di Sarra, A., Di Iorio, T., Cacciani, M., Fiocco, G., and Fua, D.: Saharan dust profiles measured by lidar
568  at Lampedusa, J. Geophys. Res. Atmos., 106, 10335-10347, 10.1029/2000jd900734, 2001.

569 Froyd, K. D., Murphy, D. M., Lawson, P., Baumgardner, D., and Herman, R. L.: Aerosols that form
570  subvisible cirrus at the tropical tropopause, Atmos. Chem. Phys., 10, 209-218, doi: 10.5194/acp-10-
571  209-2010, 2010.

572 Froyd, K. D., Murphy, D. M., Brock, C. A., Campuzano-Jost, P., Dibb, J. E., Jimenez, J. L., Kupc, A.,
573  Middlebrook, A. M., Schill, G. P., Thornhill, K. L., Williamson, C. J., Wilson, J. C., and Ziemba, L.
574  D.: A new method to quantify mineral dust and other aerosol species from aircraft platforms using
575  single-particle mass spectrometry, Atmos. Meas. Tech., 12, 6209-6239, doi: 10.5194/amt-12-6209-
576  2019, 2019.

577 Froyd, K. D., Yu, P. F., Schill, G. P., Brock, C. A., Kupc, A., Williamson, C. J., Jensen, E. J., Ray, E.,
578  Rosenlof, K. H., Bian, H. S., Darmenov, A. S., Colarco, P. R., Diskin, G. S., Bui, T., and Murphy, D.
579  M.: Dominant role of mineral dust in cirrus cloud formation revealed by global-scale measurements,
580  Nat. Geosci., 15, 177-+, doi: 10.1038/s41561-022-00901-w, 2022.

581 Ginoux, P., Chin, M., Tegen, I., Prospero, J. M., Holben, B., Dubovik, O., and Lin, S. J.: Sources and
582  distributions of dust aerosols simulated with the GOCART model, J. Geophys. Res. Atmos., 106,
583  20255-20273, doi: 10.1029/2000jd000053, 2001.

584 Grell, G. A. and Freitas, S. R.: A scale and aerosol aware stochastic convective parameterization for
585  weather and air quality modeling, Atmos. Chem. Phys., 14, 5233-5250, doi: 10.5194/acp-14-5233-
586  2014, 2014.

587 Grousset, F. E., Ginoux, P., Bory, A., and Biscaye, P. E.: Case study of a Chinese dust plume reaching
588  the French Alps, Geophys. Res. Lett., 30, doi: 10.1029/2002gl016833, 2003.

589 Hopfner, M., Ungermann, J., Borrmann, S., Wagner, R., Spang, R., Riese, M., Stiller, G., Appel, O.,
590  Batenburg, A. M., Bucci, S., Cairo, F., Dragoneas, A., Friedl-Vallon, F., Hunig, A., Johansson, S.,
591  Krasauskas, L., Legras, B., Leisner, T., Mahnke, C., Mohler, O., Molleker, S., Muller, R., Neubert, T.,
592  Orphal, J., Preusse, P., Rex, M., Saathoff, H., Stroh, F., Weigel, R., and Wohltmann, I.: Ammonium
593  nitrate particles formed in upper troposphere from ground ammonia sources during Asian monsoons,
594  Nat. Geosci., 12, 608-+, doi: 10.1038/s41561-019-0385-8, 2019.

595 Hara, Y., Yumimoto, K., Uno, I., Shimizu, A., Sugimoto, N., Liu, Z., and Winker, D.: Asian dust outflow
596  in the PBL and free atmosphere retrieved by NASA CALIPSO and an assimilated dust transport model,
597  Atmos. Chem. Phys., 9, 1227–1239, 2009.

598 Huneeus, N., Schulz, M., Balkanski, Y., Griesfeller, J., Prospero, J., Kinne, S., Bauer, S., Boucher, O.,

599   Chin, M., Dentener, F., Diehl, T., Easter, R., Fillmore, D., Ghan, S., Ginoux, P., Grini, A., Horowitz,
600   L., Koch, D., Krol, M. C., Landing, W., Liu, X., Mahowald, N., Miller, R., Morcrette, J. J., Myhre, G.,
601   Penner, J., Perlwitz, J., Stier, P., Takemura, T., and Zender, C. S.: Global dust model intercomparison
602   in AeroCom phase I, Atmos. Chem. Phys., 11, 7781-7816, doi: 10.5194/acp-11-7781-2011, 2011.
603   Karyampudi, V. M.: A detailed synoptic-scale study of the structure, dynamics, and radiative effects of
604   the Saharan air layer over the eastern tropical Atlantic during the GARP Atlantic tropical experiment,
605   1979.
606   Karyampudi, V. M., Palm, S. P., Reagen, J. A., Fang, H., Grant, W. B., Hoff, R. M., Moulin, C., Pierce,
607   H. F., Torres, O., Browell, E. V., and Melfi, S. H.: Validation of the Saharan Dust Plume Conceptual
608   Model Using Lidar, Meteosat, and ECMWF Data, Bull. Am. Meteorol. Soc., 80, 1045–1076, doi:
609   10.1175/1520-0477(1999)080<1045:VOTSDP>2.0.CO;2, 1999.
610   Kawai, K., Kai, K., Jin, Y., Sugimoto, N., and Batdorj, D.: Dust Event in the Gobi Desert on 22-23 May
611   2013: Transport of Dust from the Atmospheric Boundary Layer to the Free Troposphere by a Cold
612   Front, Sola, 11, 156-159, doi: 10.2151/sola.2015-035, 2015.
613   Kawai, K., Kai, K., Jin, Y., Sugimoto, N., and Batdorj, D.: Lidar Network Observation of Dust Layer
614   Development over the Gobi Desert in Association with a Cold Frontal System on 22-23 May 2013, J.
615   Meteorolog. Soc. Jpn., 96, 255-268, doi: 10.2151/jmsj.2018-023, 2018.
616   Kim, D., Chin, M., Yu, H. B., Pan, X. H., Bian, H. S., Tan, Q., Kahn, R. A., Tsigaridis, K., Bauer, S. E.,
617   Takemura, T., Pozzoli, L., Bellouin, N., and Schulz, M.: Asian and Trans-Pacific Dust: A Multimodel
618   and Multiremote Sensing Observation Analysis, J. Geophys. Res. Atmos., 124, 13534-13559, doi:
619   10.1029/2019jd030822, 2019.
620   Kawai, K., Matsui, H., Tobo, Y.: High Potential of Asian Dust to Act as Ice Nucleating Particles in Mixed-
621   Phase Clouds Simulated With a Global Aerosol-Climate Model, J. Geophys. Res. Atmos., 126, doi:
622   10.1029/2020JD034263, 2021.
623   Kim, D., Chin, M., Yu, H. B., Diehl, T., Tan, Q., Kahn, R. A., Tsigaridis, K., Bauer, S. E., Takemura, T.,
624   Pozzoli, L., Bellouin, N., Schulz, M., Peyridieu, S., Chedin, A., and Koffi, B.: Sources, sinks, and
625   transatlantic transport of North African dust aerosol: A multimodel analysis and comparison with
626   remote sensing data, J. Geophys. Res. Atmos., 119, 6259-6277, doi: 10.1002/2013jd021099, 2014.
627   Knippertz, P. and Todd, M. C.: Mineral dust aerosols over the Sahara: Meteorological controls on
628   emission and transport and implications for modeling, Rev. Geophys., 50, doi: 10.1029/2011rg000362,
629   2012.
630   Kok J. F., Adebiyi, A. A., Albani S., et al. : Contribution of the world's main dust source regions to the
631   global cycle of desert dust, Atmos. Chem. Phys., 21, 8169-8193, doi: 10.5194/acp-21-8169-2021, 2021.
632   Levin, Z., Ganor, E., and Gladstein, V.: The Effects of Desert Particles Coated with Sulfate on Rain
633   Formation in the Eastern Mediterranean, J. Appl. Meteorol. Climatol., 35, 1511–1523,
634   doi:10.1175/1520-0450(1996)035<1511:TEODPC>2.0.CO;2, 1996.
635   Lambert, F., Tagliabue, A., Shaffer, G., Lamy, F., Winckler, G., Farias, L., Gallardo, L., and De Pol-Holz,
636   R.: Dust fluxes and iron fertilization in Holocene and Last Glacial Maximum climates, Geophys. Res.
637   Lett., 42, 6014-6023, doi: 10.1002/2015gl064250, 2015.
638   Mahowald, N. M., Baker, A. R., Bergametti, G., Brooks, N., Duce, R. A., Jickells, T. D., Kubilay, N.,
639   Prospero, J. M., and Tegen, I.: Atmospheric global dust cycle and iron inputs to the ocean, Global
640   Biogeochem. Cy., 19(4), GB4025, doi:10.1029/2004GB002402, 2005.
641   Mahowald, N. M., Engelstaedter, S., Luo, C., Sealy, A., Artaxo, P., Benitez-Nelson, C., Bonnet, S., Chen,
642   Y., Chuang, P. Y., Cohen, D. D., Dulac, F., Herut, B., Johansen, A. M., Kubilay, N., Losno, R.,

643   Maenhaut, W., Paytan, A., Prospero, J. A., Shank, L. M., and Siefert, R. L.: Atmospheric Iron
644   Deposition: Global Distribution, Variability, and Human Perturbations, Annual Review of Marine
645   Science, 1, 245-278, doi: 10.1146/annurev.marine.010908.163727, 2009.
646   Mahowald, N., Albani, S., Kok, J. F., Engelstaeder, S., Scanza, R., Ward, D. S., and Flanner, M. G.: The
647   size distribution of desert dust aerosols and its impact on the Earth system, Aeolian Res., 15, 53-71,
648   10.1016/j.aeolia.2013.09.002, 2014.
649   Maloney, C., Toon, B., Bardeen, C., Yu, P. F., Froyd, K., Kay, J., and Woods, S.: The Balance Between
650   Heterogeneous and Homogeneous Nucleation of Ice Clouds Using CAM5/CARMA, J. Geophys. Res.
651   Atmos., 127, doi: 10.1029/2021jd035540, 2022.
652   Marticorena, B. and Bergametti, G.: Modeling the atmospheric dust cycle: 1. Design of a soil-derived
653   dust emission scheme, J. Geophys. Res. Atmos., 100, 16415–16430, 1995.
654   Mohamed, A. B. and Frangi, J.: Results from ground-based monitoring of spectral aerosol optical
655   thickness and horizontal extinction: Some specific characteristics of dusty Sahelian atmospheres, J.
656   Appl. Meteorol. Climatol., 25, 1807–1815, 1986.
657   Murayama, T., Sugimoto, N., Uno, I., Kinoshita, K., Aoki, K., Hagiwara, N., Liu, Z. Y., Matsui, I., Sakai,
658   T., Shibata, T., Arao, K., Sohn, B. J., Won, J. G., Yoon, S. C., Li, T., Zhou, J., Hu, H. L., Abo, M.,
659   Iokibe, K., Koga, R., and Iwasaka, Y.: Ground-based network observation of Asian dust events of April
660   1998 in east Asia, J. Geophys. Res. Atmos., 106, 18345-18359, doi: 10.1029/2000jd900554, 2001.
661   Murphy, D. J.: The future of oil PALM as a major global crop: opportunities and challenges, Journal of
662   Oil Palm Research, 26, 1-24, 2014.
663   Murphy, D. M., Middlebrook, A. M., and Warshawsky, M.: Cluster analysis of data from the Particle
664   Analysis by Laser Mass Spectrometry (PALMS) instrument, Aerosol Science and Technology, 37, 382-
665   391, doi: 10.1080/02786820300971, 2003.
666   Murphy, D. M., Cziczo, D. J., Froyd, K. D., Hudson, P. K., Matthew, B. M., Middlebrook, A. M., Peltier,
667   R. E., Sullivan, A., Thomson, D. S., and Weber, R. J.: Single-particle mass spectrometry of tropospheric
668   aerosol particles, J. Geophys. Res. Atmos., 111, doi: 10.1029/2006jd007340, 2006.
669   Murphy, D. M., Froyd, K. D., Bourgeois, I., Brock, C. A., Kupc, A., Peischl, J., Schill, G. P., Thompson,
670   C. R., Williamson, C. J., and Yu, P. F.: Radiative and chemical implications of the size and composition
671   of aerosol particles in the existing or modified global stratosphere, Atmos. Chem. Phys., 21, 8915-
672   8932, doi: 10.5194/acp-21-8915-2021, 2021.
673   Nazaryan, H., McCormick, M. P., and Menzel, W. P.: Global characterization of cirrus clouds using
674   CALIPSO data, Journal of Geophysical Research-Atmospheres, 113, doi: 10.1029/2007jd009481,
675   2008.
676   Prasad, A. K. and Singh, R. P.: Changes in aerosol parameters during major dust storm events (2001-
677   2005) over the Indo-Gangetic Plains using AERONET and MODIS data, J. Geophys. Res. Atmos., 112,
678   doi: 10.1029/2006jd007778, 2007.
679   Prospero, J. M.: Mineral aerosol transport to the Pacific Ocean, Chem. Oceanogr., 10, 188–218, 1989.
680   Prospero, J. M.: The atmospheric transport of particles to the ocean, Part. Flux Ocean, 57, 19–52, 1996.
681   Prospero, J. M. and Bonatti, E.: Continental dust in the atmosphere of the Eastern Equatorial Pacific, J.
682   Geophys. Res., 74, 3362–3371, https://doi.org/10.1029/JC074i013p03362, 1969.
683   Prospero, J. M. and Lamb, P. J.: African droughts and dust transport to the Caribbean: Climate change
684   implications, Science, 302, 1024-1027, doi: 10.1126/science.1089915, 2003.
685   Prospero, J. M. and Nees, R. T.: Impact of the North African drought and El Nino on mineral dust in the
686   Barbados trade winds, Nature, 320, 735–738, 1986.

687 Pu, B. and Ginoux, P.: How reliable are CMIP5 models in simulating dust optical depth?, Atmos. Chem.
688   Phys., 18, 12491-12510, doi: 10.5194/acp-18-12491-2018, 2018.
689 Rodriguez, S., Alastuey, A., and Querol, X.: A review of methods for long term in situ characterization
690   of aerosol dust, Aeolian Research, 6, 55-74, doi: 10.1016/j.aeolia.2012.07.004, 2012.
691 Rosenfeld, D., Rudich, Y., and Lahav, R.: Desert dust suppressing precipitation: A possible desertification
692   feedback loop, Proceedings of the National Academy of Sciences of the United States of America, 98,
693   5975-5980, doi: 10.1073/pnas.101122798, 2001.
694 Sassen, K., Wang, Z., and Liu, D.: Global distribution of cirrus clouds from CloudSat/Cloud-Aerosol
695   Lidar and Infrared Pathfinder Satellite Observations (CALIPSO) measurements, J. Geophys. Res.
696   Atmos., 113, doi: 10.1029/2008jd009972, 2008.
697 Satheesh, S. K. and Moorthy, K. K.: Radiative effects of natural aerosols: A review, Atmos. Environ., 39,
698   2089-2110, 10.1016/j.atmosenv.2004.12.029, 2005.
699 Schulz, M., Prospero, J. M., Baker, A. R., Dentener, F., Ickes, L., Liss, P. S., Mahowald, N. M., Nickovic,
700   S., Garcia-Pando, C. P., Rodriguez, S., Sarin, M., Tegen, I., and Duce, R. A.: Atmospheric Transport
701   and Deposition of Mineral Dust to the Ocean: Implications for Research Needs, Environ. Sci. Technol.,
702   46, 10390-10404, doi: 10.1021/es300073u, 2012.
703 Shindell, D. T., Lamarque, J. F., Schulz, M., Flanner, M., Jiao, C., Chin, M., Young, P. J., Lee, Y. H.,
704   Rotstayn, L., Mahowald, N., Milly, G., Faluvegi, G., Balkanski, Y., Collins, W. J., Conley, A. J.,
705   Dalsoren, S., Easter, R., Ghan, S., Horowitz, L., Liu, X., Myhre, G., Nagashima, T., Naik, V., Rumbold,
706   S. T., Skeie, R., Sudo, K., Szopa, S., Takemura, T., Voulgarakis, A., Yoon, J. H., and Lo, F.: Radiative
707   forcing in the ACCMIP historical and future climate simulations, Atmos. Chem. Phys., 13, 2939-2974,
708   doi: 10.5194/acp-13-2939-2013, 2013.
709 Sokolik, I. N. and Toon, O. B.: Direct radiative forcing by anthropogenic airborne mineral aerosols,
710   Nature, 381, 681-683, 10.1038/381681a0, 1996.
711 Sokolik, I. N. and Toon, O. B.: Incorporation of mineralogical composition into models of the radiative
712   properties of mineral aerosol from UV to IR wavelengths, J. Geophys. Res. Atmos., 104, 9423–9444,
713   1999.
714 Spanu, A., Dollner, M., Gasteiger, J., Bui, T. P., and Weinzierl, B.: Flow-induced errors in airborne in situ
715   measurements of aerosols and clouds, Atmos. Meas. Tech., 13, 1963-1987, doi: 10.5194/amt-13-1963-
716   2020, 2020.
717 Stith, J. L., Ramanathan, V., Cooper, W. A., Roberts, G. C., DeMott, P. J., Carmichael, G., Hatch, C. D.,
718   Adhikary, B., Twohy, C. H., Rogers, D. C., Baumgardner, D., Prenni, A. J., Campos, T., Gao, R.,
719   Anderson, J., and Feng, Y.: An overview of aircraft observations from the Pacific Dust Experiment
720   campaign, J. Geophys. Res. Atmos., 114, doi: 10.1029/2008jd010924, 2009.
721 Su, L. and Toon, O. B.: Numerical simulations of Asian dust storms using a coupled climate-aerosol
722   microphysical model, J. Geophys. Res. Atmos., 114, doi: 10.1029/2008jd010956, 2009.
723 Su, L. and Toon, O. B.: Saharan and Asian dust: similarities and differences determined by CALIPSO,
724   AERONET, and a coupled climate-aerosol microphysical model, Atmos. Chem. Phys., 11, 3263-3280,
725   doi: 10.5194/acp-11-3263-2011, 2011.
726 Tanaka, T. Y., Kurosaki, Y., Chiba, M., Matsumura, T., Nagai, T., Yamazaki, A., Uchiyama, A.,
727   Tsunematsu, N., and Kai, K.: Possible transcontinental dust transport from North Africa and the Middle
728   East to East Asia, Atmos. Environ., 39, 3901–3909, doi: 10.1016/j.atmosenv.2005.03.034, 2005.
729 Tegen, I. and Lacis, A. A.: Modeling of particle size distribution and its influence on the radiative
730   properties of mineral dust aerosol, J. Geophys. Res. Atmos., 101, 19237-19244, 10.1029/95jd03610,

731   1996

732   Tegen, I. and Schepanski, K.: The global distribution of mineral dust, IOP Conf. Ser. Earth Environ. Sci.,

733   7, 012001, doi: 10.1088/1755-1307/7/1/012001, 2009.

734   Textor, C., Schulz, M., Guibert, S., Kinne, S., Balkanski, Y., Bauer, S., Berntsen, T., Berglen, T., Boucher,

735   O., Chin, M., Dentener, F., Diehl, T., Easter, R., Feichter, H., Fillmore, D., Ghan, S., Ginoux, P., Gong,

736   S., Kristjansson, J. E., Krol, M., Lauer, A., Lamarque, J. F., Liu, X., Montanaro, V., Myhre, G., Penner,

737   J., Pitari, G., Reddy, S., Seland, O., Stier, P., Takemura, T., and Tie, X.: Analysis and quantification of

738   the diversities of aerosol life cycles within AeroCom, Atmos. Chem. Phys., 6, 1777-1813, doi:

739   10.5194/acp-6-1777-2006, 2006.

740   Thomason, L. W. and Vernier, J. P.: Improved SAGE II cloud/aerosol categorization and observations of

741   the Asian tropopause aerosol layer: 1989-2005, Atmos. Chem. Phys., 13, 4605-4616, doi: 10.5194/acp-

742   13-4605-2013, 2013.

743   Toon, O. B., Turco, R. P., Westphal, D., Malone, R., and Liu, M.: A Multidimensional Model for Aerosols:

744   Description of Computational Analogs, J. Atmospheric Sci., 45, 2123–2144, doi: 10.1175/1520-

745   0469(1988)045<2123:AMMFAD>2.0.CO;2, 1988.

746   Vernier, J. P., Thomason, L. W., and Kar, J.: CALIPSO detection of an Asian tropopause aerosol layer,

747   Geophys. Res. Lett., 38, doi: 10.1029/2010gl046614, 2011.

748   Vernier, J. P., Fairlie, T. D., Natarajan, M., Wienhold, F. G., Bian, J., Martinsson, B. G., Crumeyrolle, S.,

749   Thomason, L. W., and Bedka, K. M.: Increase in upper tropospheric and lower stratospheric aerosol

750   levels and its potential connection with Asian pollution, J. Geophys. Res. Atmos., 120, 1608-1619, doi:

751   10.1002/2014jd022372, 2015.

752   Vernier, J. P., Fairlie, T. D., Deshler, T., Ratnam, M. V., Gadhavi, H., Kumar, B. S., Natarajan, M., Pandit,

753   A. K., Raj, S. T. A., Kumar, A. H., Jayaraman, A., Singh, A. K., Rastogi, N., Sinha, P. R., Kumar, S.,

754   Tiwari, S., Wegner, T., Baker, N., Vignelles, D., Stenchikov, G., Shevchenko, I., Smith, J., Bedka, K.,

755   Kesarkar, A., Singh, V., Bhate, J., Ravikiran, V., Rao, M. D., Ravindrababu, S., Patel, A., Vernier, H.,

756   Wienhold, F. G., Liu, H., Knepppp, T. N., Thomason, L., Crawford, J., Ziembmba, L., Moore, J.,

757   Crumeyrolle, S., Williamson, M., Berthet, G., Jegou, F., and Renard, J. B.: BATAL The Balloon

758   Measurement Campaigns of the Asian Tropopause Aerosol Layer, Bull. Am. Meteorol. Soc., 99, 955-

759   973, doi: 10.1175/bams-d-17-0014.1, 2018.

760   Wang, H., Easter, R. C., Rasch, P. J., Wang, M., Liu, X., Ghan, S. J., Qian, Y., Yoon, J. H., Ma, P. L., and

761   Vinoj, V.: Sensitivity of remote aerosol distributions to representation of cloud-aerosol interactions in

762   a global climate model, Geosci. Model Dev., 6, 765-782, doi: 10.5194/gmd-6-765-2013, 2013.

763   Wang, Y. Q., Zhang, X. Y., Gong, S. L., Zhou, C. H., Hu, X. Q., Liu, H. L., Niu, T., and Yang, Y. Q.:

764   Surface observation of sand and dust storm in East Asia and its application in CUACE/Dust, Atmos.

765   Chem. Phys., 8, 545-553, doi: 10.5194/acp-8-545-2008, 2008.

766   Wiacek, A., Peter, T., Lohmann, U.: The potential influence of Asian and African mineral dust on ice,

767   mixed-phase and liquid water clouds, Atmos. Chem. Phys., 10, 8649-8667, doi: 10.5194/acp-10-8649-

768   2010, 2010.

769   Wofsy, S. C., Afshar, S., Allen, H. M., Apel, E. C., Asher, E. C., Barletta, B., Bent, J., Bian, H., Biggs, B.

770   C., Blake, D. R., Blake, N., Bourgeois, I., Brock, C. A., Brune, W. H., Budney, J. W., Bui, T. P., Butler,

771   A., Campuzano-Jost, P., Chang, C. S., Chin, M., Commane, R., Correa, G., Crounse, J. D., Cullis, P.

772   D., Daube, B. C., Day, D. A., Dean-Day, J. M., Dibb, J. E., Digangi, J. P., Diskin, G. S., Dollner, M.,

773   Elkins, J. W., Erdesz, F., Fiore, A. M., Flynn, C. M., Froyd, K. D., Gesler, D. W., Hall, S. R., Hanisco,

774   T. F., Hannun, R. A., Hills, A. J., Hintsa, E. J., Hoffman, A., Hornbrook, R. S., Huey, L. G., Hughes,

775   S., Jimenez, J. L., Johnson, B. J., Katich, J. M., Keeling, R. F., Kim, M. J., Kupc, A., Lait, L. R.,
776   Lamarque, J.-F., Liu, J., Mckain, K., Mclaughlin, R. J., Meinardi, S., Miller, D. O., Montzka, S. A.,
777   Moore, F. L., Morgan, E. J., Murphy, D. M., Murray, L. T., Nault, B. A., Neuman, J. A., Newman, P.
778   A., Nicely, J. M., Pan, X., Paplawsky, W., Peischl, J., Prather, M. J., Price, D. J., Ray, E. A., Reeves, J.
779   M., Richardson, M., Rollins, A. W., Rosenlof, K. H., Ryerson, T. B., Scheuer, E., Schill, G. P., Schroder,
780   J. C., Schwarz, J. P., St. Clair, J. M., Steenrod, S. D., Stephens, B. B., Strode, S. A., Sweeney, C.,
781   Tanner, D., Teng, A. P., Thames, A. B., Thompson, C. R., Ullmann, K., Veres, P. R., Vizenor, N., Wagner,
782   N. L., Watt, A., Weber, R., Weinzierl, B. B., et al.: ATom: Merged Atmospheric Chemistry, Trace Gases,
783   and Aerosols, ORNL DAAC, doi: 10.3334/ORNLDAAC/1581, 2018.
784   Wu, C., Lin, Z., Liu, X. : The global dust cycle and uncertainty in CMIP5 (Coupled Model
785   Intercomparison Project phase 5) models, Atmos. Chem. Phys., 20, 10401-10425, doi: 10.5194/acp-
786   20-10401-2020, 2020.
787   Yang, K., Wang, Z. E., Luo, T., Liu, X. H., and Wu, M. X.: Upper troposphere dust belt formation
788   processes vary seasonally and spatially in the Northern Hemisphere, Communications Earth &
789   Environment, 3, doi: 10.1038/s43247-022-00353-5, 2022.
790   Yu, H. B., Chin, M., Winker, D. M., Omar, A. H., Liu, Z. Y., Kittaka, C., and Diehl, T.: Global view of
791   aerosol vertical distributions from CALIPSO lidar measurements and GOCART simulations: Regional
792   and seasonal variations, J. Geophys. Res. Atmos., 115,doi: 10.1029/2009jd013364, 2010.
793   Yu, H. B., Chin, M., Bian, H. S., Yuan, T. L., Prospero, J. M., Omar, A. H., Remer, L. A., Winker, D. M.,
794   Yang, Y. K., Zhang, Y., and Zhang, Z. B.: Quantification of trans-Atlantic dust transport from seven-
795   year (2007-2013) record of CALIPSO lidar measurements, Remote Sens. Environ., 159, 232-249, doi:
796   10.1016/j.rse.2014.12.010, 2015a.
797   Yu, P. F., Toon, O. B., Bardeen, C. G., Mills, M. J., Fan, T. Y., English, J. M., and Neely, R. R.: Evaluations
798   of tropospheric aerosol properties simulated by the community earth system model with a sectional
799   aerosol microphysics scheme, J. Adv. Model. Earth Syst., 7, 865-914, doi: 10.1002/2014ms000421,
800   2015b.
801   Yu, P., Rosenlof, K. H., Liu, S., Telg, H., Thornberry, T. D., Rollins, A. W., Portmann, R. W., Bai, Z., Ray,
802   E. A., Duan, Y., Pan, L. L., Toon, O. B., Bian, J., and Gao, R.-S.: Efficient transport of tropospheric
803   aerosol into the stratosphere via the Asian summer monsoon anticyclone, Proc. Natl. Acad. Sci., 114,
804   6972–6977, doi: 10.1073/pnas.1701170114, 2017.
805   Yu, P. F., Froyd, K. D., Portmann, R. W., Toon, O. B., Freitas, S. R., Bardeen, C. G., Brock, C., Fan, T.
806   Y., Gao, R. S., Katich, J. M., Kupc, A., Liu, S., Maloney, C., Murphy, D. M., Rosenlof, K. H., Schill,
807   G., Schwarz, J. P., and Williamson, C.: Efficient In-Cloud Removal of Aerosols by Deep Convection,
808   Geophys. Res. Lett., 46, 1061-1069, doi: 10.1029/2018gl080544, 2019.
809   Zender, C. S., Miller, R. L. R. L., and Tegen, I.: Quantifying mineral dust mass budgets:Terminology,
810   constraints, and current estimates, Eos Trans. Am. Geophys. Union, 85, 509–512, doi:
811   10.1029/2004EO480002, 2004.
812   Zwaaftink, C. D. G., Grythe, H., Skov, H., and Stohl, A.: Substantial contribution of northern high-
813   latitude sources to mineral dust in the Arctic, J. Geophys. Res. Atmos., 121, 13678-13697, doi:
814   10.1002/2016jd025482, 2016.